

## Room-temperature THz detection via EIW effect based on graphite nanosheet

YAN Jiang-Wei<sup>1</sup>, ZHANG Xiao-Dong<sup>1</sup>, ZHOU Wei<sup>2</sup>, MA Wan-Li<sup>2</sup>, HU Tao<sup>2</sup>, YAO Niang-Juan<sup>2</sup>,  
JIANG Lin<sup>2</sup>, HUANG Zhi-Ming<sup>2,3,4\*</sup>

(1. Department of Applied Physics, Donghua University, Shanghai 201620, China;

2. State Key Laboratory of Infrared Physics, Shanghai Institute of Technical Physics, Chinese Academy of Sciences, Shanghai 200083, China;

3. Key Laboratory of Space Active Opto-Electronics Technology, Shanghai Institute of Technical Physics, Chinese Academy of Sciences, Shanghai 200083, China;

4. Hangzhou Institute for Advanced Study, University of Chinese Academy of Sciences, Hangzhou 310024, China)

**Abstract:** We demonstrate a room-temperature sub-terahertz photoconductive detector based on graphite nanosheet (GN) using electromagnetic induced well (EIW) effect produced in the metal-GN-metal structure. The detector achieves high performance of room-temperature THz detection. It shows a responsivity of over 20 kV/W at 0.035 THz and 11 kV/W at 0.1673 THz, as well as NEP of about 1.25 pW/Hz<sup>1/2</sup> at 0.035 THz and 2.27 pW/Hz<sup>1/2</sup> at 0.1673 THz, respectively. The results open up a new idea for graphene-based THz detection.

**Key words:** infrared physics, terahertz detection, photoconductivity, EIW effect, graphite nanosheet

## 基于石墨纳米材料的电磁诱导势阱效应的室温太赫兹探测研究

阎蒋伟<sup>1</sup>, 张晓东<sup>1</sup>, 周 炜<sup>2</sup>, 马万里<sup>2</sup>, 胡 涛<sup>2</sup>, 姚娘娟<sup>2</sup>, 江 林<sup>2</sup>, 黄志明<sup>2,3,4\*</sup>

(1. 东华大学 理学院 应用物理系, 上海 201620;

2. 中国科学院上海技术物理研究所 红外物理国家重点实验室, 上海 200083;

3. 中国科学院上海技术物理研究所 空间主动光电技术重点实验室, 上海 200083;

4. 中国科学院大学杭州高等研究院, 浙江 杭州 310024)

**摘要:** 基于石墨纳米材料, 成功制备金属-石墨-金属结构电磁诱导势阱效应室温太赫兹探测器, 实现了高性能的室温太赫兹探测。器件在 0.035 THz 的响应率达到 20 kV/W, 在 0.1673 THz 的响应率达到 11 kV/W, 器件在 0.035 THz 的噪声等效功率达到 1.25 pW/√Hz, 在 0.1673 THz 的噪声等效功率达到 2.27 pW/√Hz。我们的研究结果为石墨太赫兹探测器提供新的思路。

**关键词:** 红外物理; 太赫兹探测; 光电导; 电磁诱导势阱效应; 石墨纳米片

中图分类号: O511; O782

文献标识码: A

### Introduction

Graphene has several advantages compared with other materials<sup>[1-3]</sup>. It is gapless, which enables strong broadband spectral absorption from terahertz to infrared. It also exhibits ultrafast carrier dynamics<sup>[4, 5]</sup> and high carrier mobility, which allows ultrafast conversion of pho-

tons or plasmons to electrical current or voltage<sup>[6, 7]</sup>. The advantage of high carrier mobility makes graphene a hot research focus in many fields, especially the development of photodetector. Graphene has been used in applications including optical modulators<sup>[8]</sup>, optical frequency combs<sup>[9]</sup>, plasmonic devices<sup>[10]</sup> and ultrafast lasers<sup>[11]</sup>. Moreover, graphene is compatible with the highly mature

**Received date:** 2022-02-03, **revised date:** 2022-02-24

**收稿日期:** 2022-02-03, **修回日期:** 2022-02-24

**Foundation items:** Supported by the National Natural Science Foundation of China (61625505, 12134016); Chinese Academy of Sciences (ZDBS-LY-JSC025); Shanghai Municipal Science and Technology Major Project (2019SHZDZX01).

**Biography:** Yan Jiang-Wei (1994—), male, Taiyuan, Shanxi Province, Postgraduate, research is mainly about photoelectric materials and devices, E-mail: 15000838572@163.com

\* **Corresponding author:** Email: zmhuang@mail.sitp.ac.cn

silicon-based platform for electronics and photonics, making it a promising candidate for cost-effective and large-scale integration into optoelectronic networks and multipixel CMOS read-out circuits<sup>[12, 13]</sup>. However, single layer or multilayer graphene only has weak optical absorption. For a few layered graphene detectors, the optical absorption is limited since most of the terahertz radiation penetrates through the sensitive element. In contrast, graphite nanosheet (GN) has hundreds of layers or more in thickness. Therefore, most of the terahertz waves irradiated on the detector can be absorbed by graphite nanosheet except for a small part of reflection, which can significantly improve the device quantum efficiency and increase the responsivity of detectors.

THz technology has attracted great attention in recent years, because of its wide application in many fields, such as medicine, biology, weather forecast, and environmental protection. Different detection mechanisms have been proposed<sup>[14-18]</sup>. Cai, X. demonstrated a graphene thermoelectric terahertz photodetector with sensitivity exceeding 700 V/W and noise-equivalent power less than 20 pW/ $\sqrt{\text{Hz}}$ <sup>[19]</sup>. Recently, high sensitivity detection of terahertz waves was achieved with a graphene nanomesh as grating to improve the coupling efficiency of the incident terahertz waves and using a graphene nanostructure energy gap to enhance the excitation of plasmon. The sensitivity of the detector is 2.5 A/W<sup>[20]</sup>. A hot carrier-assisted photoconduction has been reported in homogeneous graphene, which shows sensitivity over  $4 \times 10^3$  V/W and noise-equivalent power less than 20 pW/ $\sqrt{\text{Hz}}$  at room temperature<sup>[21]</sup>. In this paper, a novel photoconductivity mechanism for THz detection is proven to be applicable for the design of a metal-GN-metal detector<sup>[22, 23]</sup>: Consider a metal-GN-metal structure as shown in Figure 1. The spacing length and the width are  $a$  and  $b$ , respectively. The thickness of the GN is  $d$ . In the metal-GN-metal structure, there are two electric field configurations that are either symmetric or anti-symmetric with respect to the electrodes. Only anti-symmetric one has contribution to form potential wells and further trap carriers. The variation of the electron concentration can be further written according to the deduction by the electromagnetic induced well (EIW) theory<sup>[22]</sup>. When THz wave irradiates the GN mesa, electrons are driven from metals into the GN mesa. An EIW is generated by anti-symmetric electric field between the two metallic contacts and traps electrons from the metals in the well, then the conductivity of the GN mesa is changed and voltage signal is able to be detected. By taking advantage of the EIW photoconductivity effect, we achieve room-temperature sub-THz detection based on graphite nanosheets with sensitivity exceeding  $11 \times 10^3$  V/W (100 A/W) and noise-equivalent power of 2.27 pW/ $\sqrt{\text{Hz}}$  at room temperature.

## 1 Experiment

The graphite nanosheets were peeled off from bulk graphite crystal by the way of micro-mechanical exfolia-

tion using scotch type. After that, the nanosheets were transferred onto a high resistance Si substrate ( $> 10000 \Omega \cdot \text{cm}$ ). The nanosheets could be identified by the optical microscope and the thickness of the flakes could be measured by atomic force microscope (AFM) as shown in Figure 2.

Ti (30 nm), and Au (100 nm) electrodes were evaporated on the top of the GN. The evaporation mask was fabricated using standard UV lithography. Metal-GN-metal structure was used to form an electromagnetic induced well (EIW) in graphite nanosheets. Both the top and the two side walls of the GN were covered in order to prevent the leakage of electromagnetic waves from the two sides and achieve a large optical gain. The width of the metal antenna was 0.5 mm and the total length of the metal antenna was 4 mm. The active receiving area of the device was  $11 \times 42 \mu\text{m}^2$  and the thickness was 146 nm on average. The gap length (11  $\mu\text{m}$ ) was close to the distance designed.

The Terahertz test system is established for sub-THz detection, as shown in Figure 3. In order to measure the sensitivity of the detector precisely, we use the solid-state frequency multiplication source produced by VDI Corporation (USA) that can emit continuous terahertz waves to radiate terahertz waves of 165-173 GHz. We also use lock-in amplifier to record the photo-response of commercial detector. The distance  $d$  between THz source and our detector, the horn diameter ( $D$ ) and the detection wavelength ( $\lambda$ ) are set up to satisfy the condition:  $d \gg 2D^2/\lambda$ . And the effective receiving area of the detector is far less than the area of the diaphragm. An adjustable diaphragm is placed in front of the commercial to calibrate the uniformity of the spot. We adjust the size of the diaphragm to get different voltage responses. The test data shows that the voltage response of the commercial is approximately linear to the area of the diaphragm, so we consider the field contribution is uniform. The power density of microwave source (20-40 GHz) is estimated by the total output power and the microwave filed area in the place of the detector when we ignore the transmission efficiency and microwave field uniformity. The power density is 0.88 mW/cm<sup>2</sup> for 0.035 THz and 0.15 mW/cm<sup>2</sup> for 0.1673 THz, respectively. The polarization direction of the incident THz wave which is specified in the experimental set up is perpendicular to the metal surface in order to get the high responsivity.

## 2 Results and discussion

### 2.1 Performance of detector

Figure 4 (a) shows the I-V curve of the detector. The linear fit of I-V curve indicates a good ohmic contact between graphene and metal electrodes. Therefore, the depolarization field and the resistance of the interfaces can be ignored. The derived resistance of the device is about 110  $\Omega$ .

It is important to confirm the effective receiving area for estimating the performance of the detector. In all kinds of THz detector based on graphene, different methods of calculating the effective receiving area have been

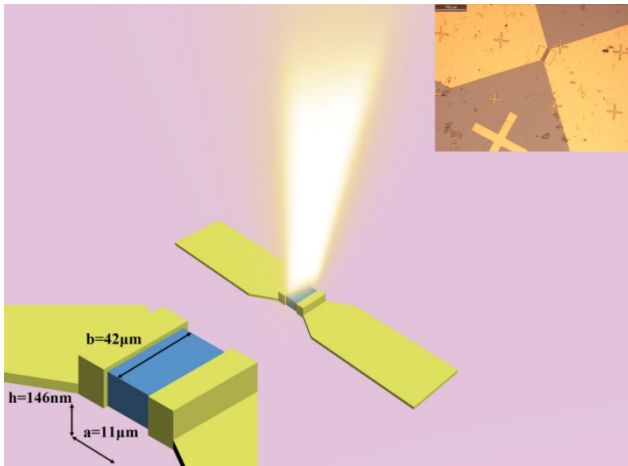


Fig. 1 The schematic diagram of the metal-GN-metal structure  
图1 金属-石墨-金属结构器件的示意图

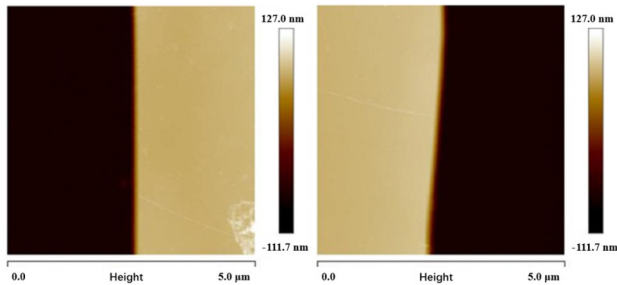


Fig. 2 AFM images of two opposite interfaces between graphene nanosheet and Si substrate, the two-step heights between graphene nanosheets and high resistance Si are calculated by the difference of the maximum peak height and minimum peak height, the two-step heights are 148 nm (left picture) and 144 nm (right picture) respectively

图2 石墨纳米材料与高电阻 Si 之间的两个台阶高度通过最大峰高和最小峰高的差值计算,两个台阶高度分别为 148 nm(左图)和 144 nm(右图)

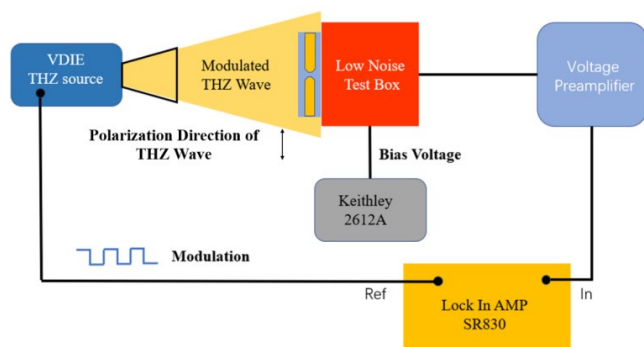


Fig. 3 The schematic diagram of Terahertz test system  
图3 太赫兹测试系统示意图

used. In plasma-wave-assisted mechanism in Field effect transistors (FETs), photoinduced voltage is derived from the amplitude of radiation induced modulation of the source to gate voltage, which is originating from the metal antenna, so the antenna effect must be considered<sup>[14, 24, 25]</sup> (diffraction limited area is commonly used to

get a lower responsivity<sup>[26, 27]</sup>). However, for photo-thermoelectric effect (PTE), the thermoelectric voltage (Seebeck effect) is induced by the temperature gradient caused by nonuniform illumination. For PTE detectors, the effective receiving area is considered to be the real material area, and diffraction limited area is also used as an estimation<sup>[19, 28]</sup>.

Here we measure the resistance change of the GN, which depends on the change in carrier mobility or carrier concentration. In the latter discussion, we exclude the bolometric effect of this detector, so the resistance change comes from variation of carrier concentration. It is caused by the electrons trapped in the GN by the EIW. Thus, we consider the effective receiving area should be the GN material area between the electrodes. In order to further prove this point, two points have been stated: (1) we have made the semiconductor devices with different sizes. It is found that the voltage response is proportional to the material area and is independent on the antenna area (not shown here). (2) we have considered the portion of metal on the mesa, because the electrons wrapped in the GN come from the metals. This small part of metal contributes to the increase in the conductance of the detector and is small enough to be ignored during calculating the effective receiving area. Of course, the metal antenna is supposed to be considered because of its contribution to the increasing of power density which is shown as gain factor ( $G$ ). Therefore, we calculate the responsivity according to formula (1) as follows:

$$R_v = \frac{\sqrt{2} \pi \times V_0}{2 \times S \times P_0 \times G} \quad (1)$$

In formula (1),  $\sqrt{2} \pi/2$  originates from the Fourier transform of the square-wave modulated signal detected as rms value with a lock-in amplifier<sup>[21]</sup>.  $V_0$  is the voltage response signal of the detector to sub-terahertz wave.  $P_0$  is the power density of incident light and  $S$  is the effective receiving area of the detector.  $G$  is the gain factor of the structure. Here, we refer to the gain of 0.8 at 0.15 THz and 1.73 at 0.0375 THz in Ref. [22] using software simulations.

As shown in Figure 4(b) and Figure 4(c), the peak of responsivity appears at 0.035 THz and reaches around 20 kV/W in the 0.02-0.04 THz, while another peak value appears at 0.1673 THz and reaches around 11 kV/W in the 0.165-0.173 THz. As shown in Figure 4(b), the regular fluctuation between 0.034-0.036 THz is due to the interference caused by the thickness of Si substrate, which is about 0.4 mm. The oscillation with faster period in Figure 4(c) is resulted from the interference caused by the distance between the RF source and Si substrate, which is about 200 mm.

NEP is a key parameter to evaluate the performance of the detectors in consideration of noise characteristic, as the noise of the detector should be suppressed. The noise signal of our detector was recorded by a spectrum analyzer (MODEL SR 770). The modulation frequency was set to cover from 250 Hz to 100 kHz, and the bandwidth was 250 Hz. Firstly, we measured the short noise ( $N_s$ ) when the circuit was shorted, and then connected

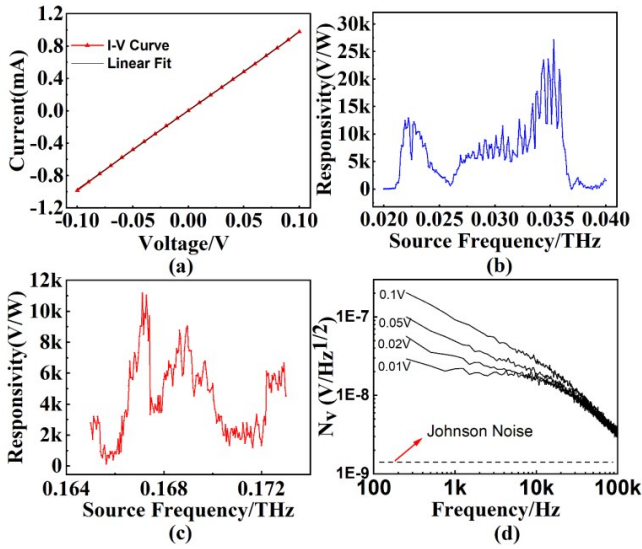


Fig. 4 (a) The I-V curve of the detector, (b-c) the responsivity of the detector at the source frequency of 0.02-0.04 THz and 0.165-0.173 THz with the bias voltage of 0.1 V, respectively, (d) the noise spectrum at the frequency from 250 Hz to 100 kHz with the bias voltage from 0.1 V to 0.01 V

图4 (a)器件的IV特性曲线,(b-c)器件在偏置电压为0.1V时工作在源频率分别为0.02~0.04 THz与0.165~0.173 THz下的响应率光谱曲线,(d)器件在不同偏置电压下的250 Hz到100 kHz噪声频谱图

the detector into the circuit for measuring the total noise ( $N_a$ ), finally we calculated the detector noise ( $N_v$ ) by using a simple mean square root formula<sup>[29]</sup>:

$$N_v = \sqrt{N_a^2 - N_i^2} \quad (2)$$

NEP is calculated by formula (3) as follows:

$$NEP = \frac{N_v}{R_v} \quad (3)$$

In this formula,  $R_v$  is the responsivity of the detector mentioned above. Different noise spectra of the detector were measured by varying the operating voltage (0.01 V, 0.02 V, 0.05 V, and 0.1 V). As shown in Figure 4 (d), the total noise ( $N_a$ ) was dominated by the detector in low  $f$ , since the  $N_v$ - $f$  curve varies with increasing bias voltage ( $V_B$ ). In contrast, the  $N_v$ - $f$  curves at different  $V_B$  overlap with each other in the range of 20 kHz to 100 kHz, indicating the dominating factor of preamplifier noise. The  $N_v$ - $f$  character of the detector fits well with the  $1/f$  law at low  $f$ , which is more than an order larger than the Johnson noise. The detector noise ( $N_v$ ) is 92 nV/ $\sqrt{\text{Hz}}$  at 1 kHz, and 25 nV/ $\sqrt{\text{Hz}}$  at 10 kHz. During the calculation, the NEP of our detector is smaller than 4.6 pW/ $\sqrt{\text{Hz}}$  for 0.035 THz and 9.2 pW/ $\sqrt{\text{Hz}}$  for 0.1673 THz at 1 kHz. Under the same modulation frequency of 10 kHz, the NEP of the detector is about 1.25 pW/ $\sqrt{\text{Hz}}$  for 0.035 THz and 2.27 pW/ $\sqrt{\text{Hz}}$  for 0.1673 THz.

The time constant represents the speed of a detector responding to an incident electromagnetic wave. The value of time constant is defined as the time from the moment the incident light irradiated onto the surface of the detector to the moment that the signal reaches 63 percent

of the maximum rise (fall).

$$i_s(t) = i_\infty [1 - \exp(-t/\tau)] \quad (4)$$

When  $i_s(t) = 0.63i_\infty$ ,  $t = \tau$ .  $\tau$  is the time constant. Here, we record the waveform at a modulation frequency of 1 kHz by an oscilloscope and the waveform is shown in Figure 5(a). By using the impulse response method, we calculate the response time constant of the detector, which is approximately 700 ns for the rise edge and 1.5  $\mu\text{s}$  for the drop edge.

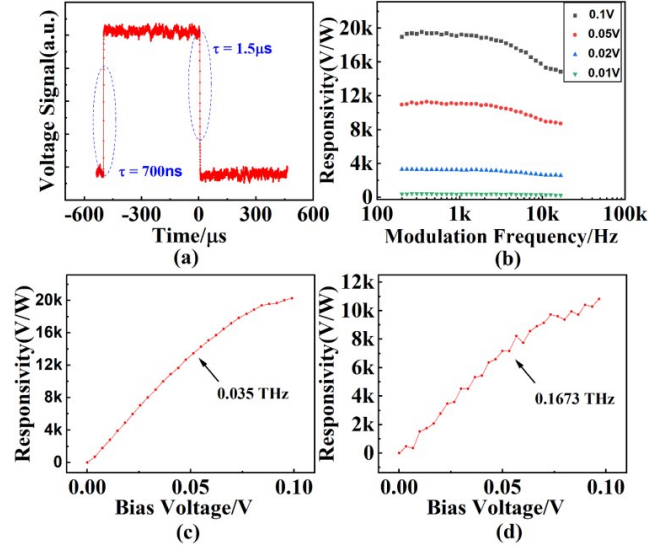


Fig. 5 (a) The waveform of the detector and time constant derivation from the waveform at 0.035 THz with the modulation frequency of 1 kHz, (b) the frequency dependent responses of the detector with different bias voltage (0.01 V, 0.02 V, 0.05 V and 0.1 V) at the source frequency of 0.035 THz, (c-d) the responsivity of the detector under different bias voltages at the source frequency of 0.035 THz and 0.1673 THz with the modulation frequency of 1 kHz, respectively

图5 (a)器件工作在太赫兹源0.035 THz,调制频率1 kHz时的响应波形与时间常数,(b)器件工作在太赫兹源0.035 THz时不同偏置电压(0.01 V, 0.02 V, 0.05 V and 0.1 V)下的响应率随调制频率变化曲线,(c-d)器件分别工作在太赫兹源0.035 THz和0.1673 THz,调制频率为1 kHz下的响应率随偏置电压的变化曲线

Figure 5(b) shows the response change trend of the device with modulation frequency at different bias voltages from 0.01 V to 0.1 V at 0.035 THz source radiation. As shown in Figure 5(c-d), the responsivity changes with the bias voltage at a modulation frequency of 1 kHz. Such linear dependency of the voltage response on the bias voltage can be observed in Figure 5(b-d). A significant voltage response was experimentally observed, while it could not be explained by the plasma-wave-assisted mechanism in FETs (Field Effect Transistors) nor photo-thermoelectric effect (PTE). To clarify the mechanism of the detector, we further discussed the change in resistance caused by bolometric effect.

## 2.2 Discussion on detection mechanism

Bolometric effect is an important effect in graphite and graphene, so it is necessary to confirm if the voltage response is dominated by the bolometric effect. First,



hot electron effect plays an important role in graphene and graphite. The strong e - e interactions will lead to ultrafast heating of the electron. Thus, an effective temperature  $T_e$  of electron remains higher than that of the lattice for femtosecond timescale. The electron-phonon scattering occurs for a slower time of several picoseconds. The hot electron concept described in the above is justified if the inequality relation below is satisfied with a conductor of size  $L$ :<sup>[30]</sup>

$$L_{e-e} < L < L_{e-ph} \quad , \quad (5)$$

here,  $L_{e-e} = (D\tau_{e-e})^{1/2}$  is the diffusion length of electrons for electron-electron equilibration, where  $\tau_{e-e}$  is the electron-electron scattering time and  $D = \bar{v}^2\tau_m/2$  is the diffusion constant with  $\bar{v}$  the average speed of electrons and  $\tau_m$  the momentum relaxation time.  $L_{e-ph} = (D\tau_{e-ph})^{1/2}$  is the diffusion length of electrons for electron-phonon equilibration, where  $\tau_{e-ph}$  is the electron-phonon energy relaxation time. The half of the inequality relation,  $L < L_{e-ph}$ , requires that a low rate of electron-phonon scattering, which leads to a nonequilibrium state between electrons and the lattice, yielding the effective electron temperature higher than that of the lattice. A life-time estimate of electron-phonon scattering in graphite is 7 ps for THz pulses<sup>[31]</sup>. Electron effective velocity in graphite is  $0.94 \times 10^6$  m/s in first-principles calculations<sup>[32]</sup>. We estimate  $D \approx v_F l/2$ , here  $l = v_F\tau$  is the mean free path of electrons,  $v_F = \bar{v}$  and  $\tau_m = \tau \approx \tau_{e-e} = 100$  fs<sup>[33]</sup>. Hence, we get a calculation of the diffusion length of electron  $L_{e-e} = 67$  nm and  $L_{e-ph} = 556$  nm. In our device, the channel length (11  $\mu\text{m}$ ) is much larger than the diffusion length. The rate of electron-phonon scattering is so frequent that electrons are equilibrated with the lattice, yielding the effective electron temperature equivalent to the lattice temperature. Therefore, the hot electron effect can be ruled out in this device.

Next, we made an estimation for the temperature rise in order to eliminate the bolometric effect in our detector. We neglected the thermal conductivity of the graphene material, and assumed that the photon energy was completely converted into thermal energy and the detec-

tor was in a thermally insulated state for estimating the temperature rise of the material. Thus, formula (6) can be written as follows:

$$\Delta T = \frac{\Delta Q}{mC_p} = \frac{P\Delta t}{mC_p} \quad , \quad (6)$$

where  $m$  is the mass of the material,  $C_p$  is the specific heat capacity of graphite (710 J/kg·K),  $\Delta t$  is the response time of the detector, and  $P$  is the power from the sub-THz source. Considering that the energy of the THz source can be coupled to the active element by the metal electrodes, the effective power can be enlarged because of field enhancement. The field enhancement is simulated to be close to 1 because the permittivity values of graphite and metal are close to each other. If the device is dominated by the bolometric effect, the voltage signal is estimated to be  $1.8 \times 10^{-8}$  V, which is two orders smaller than the measured value in magnitude. The large difference indicates that bolometric effect does not play an important role in this detection.

The responsivity of the device is linear with the bias voltage, which is consistent with the expected results of the EIW theory. The increasing of the bias voltage means a larger internal bias field, thus the EIW generated in the GN will wrap more electron from metal electrode, which explains the linear behavior of responsivity with bias voltage. According to the formula of EIW, the responsivity of this device is supposed to be 60.5 kV/W, which is the same order with the responsivity according to experimental data, so we consider that EIW theory is a reasonable explanation for the voltage response of the detector. Table 1 compares the performance of different graphene-based detectors<sup>[19-21, 27, 28, 34-37]</sup> and our detector has higher responsivity and lower NEP than the detectors reported.

### 3 Conclusion

In summary, a room-temperature sub-THz detector with high responsivity has been fabricated based on a simple metal-GN-metal structure. We have used graphite nanosheets to increase the optical absorption of the material. The EIW mechanism has been used to explain the

**Table 1 Comparison of responsivity and NEP of room temperature graphene or graphite nanosheet detectors designed with different mechanisms**

表1 比较基于不同探测机制的室温石墨与石墨烯探测器响应率与等效噪声功率

Detection Mechanism	Responsivity (V/W)	NEP (pW/ $\sqrt{\text{Hz}}$ )	Frequency (THz)	Effective area	Reference
EIW	11000	2.27	0.17	Real area	This work
Photoconduction assisted by hot-carriers	400	500	0.15	Real area	[21]
PTE	10	1100	2.5	Real area	[19]
PTE	105	80	1.8-4.25	Diffraction limited area	[28]
PTE	-	1000	2.8	Diffraction limited area	[34]
GFET	1.2	2000	0.29-0.38	Diffraction limited area	[27]
GFET	2.5A/W	-	3	Real area	[20]
GFET	14	515	0.6	-	[35]
GFET	30	120	3.4	Diffraction limited area	[36]
Nanoporous Graphene	-	424	1.4	-	[37]

THz detection based on the metal-GN-metal detector, while the contribution of bolometric effect has been excluded. Since the NEP performance declines slightly from 0.035 THz to 0.17 THz, it is expected that its detection performance for higher THz frequencies can be further improved by using ultrashort channel length of GN mesa, or by increasing the coupling effect between the electrodes and the GN material.

## References

- [1] Bonaccorso F, Sun Z, Hasan T, *et al.* Graphene photonics and optoelectronics [J]. *Nature Photonics*, 2010, **4** (9), 611–622.
- [2] Ferrari A C, Bonaccorso F, Fal'ko V, *et al.* Science and technology roadmap for graphene, related two-dimensional crystals, and hybrid systems [J]. *Nanoscale*, 2015, **7** (11), 4598–4810.
- [3] Suzuki D, Okamoto T, Li J, *et al.* Terahertz and infrared response assisted by heat localization in nanoporous graphene [J]. *Carbon*, 2021, **173**, 403–409.
- [4] Dawlaty J M, Shivaraman S, Chandrashekar M, *et al.* Measurement of ultrafast carrier dynamics in epitaxial graphene [J]. *Applied Physics Letters*, 2008, **92** (4), 042116.
- [5] Brida D, Tomadin A, Manzoni C, *et al.* Ultrafast collinear scattering and carrier multiplication in graphene [J]. *Nat Commun*, 2013, **4**, 1987.
- [6] Xia F N, Mueller T, Lin Y M, *et al.* Ultrafast graphene photodetector [J]. *Nat. Nanotechnol.*, 2009, **4** (12), 839–843.
- [7] Mueller T, Xia F N A, Avouris P. Graphene photodetectors for high-speed optical communications [J]. *Nature Photonics*, 2010, **4** (5), 297–301.
- [8] Liu M, Yin X B, Ulin-Avila E, *et al.* A graphene-based broadband optical modulator [J]. *Nature*, 2011, **474** (7349), 64–67.
- [9] Li H, Yan M, Wan W, *et al.* Graphene-Coupled Terahertz Semiconductor Lasers for Enhanced Passive Frequency Comb Operation [J]. *Adv Sci (Weinh)*, 2019, **6**, (20), 1900460.
- [10] Grigorenko A N, Polini M, Novoselov K S. Graphene plasmonics [J]. *Nature Photonics*, 2012, **6** (11), 749–758.
- [11] Sun Z P, Hasan T, Torrisi F, *et al.* Graphene Mode-Locked Ultrafast Laser [J]. *Acs Nano*, 2010, **4** (2), 803–810.
- [12] Gan X T, Shiue R J, Gao Y D, *et al.* Chip-integrated ultrafast graphene photodetector with high responsivity [J]. *Nature Photonics*, 2013, **7** (11), 883–887.
- [13] Pospischil A, Humer M, Furchi M M, *et al.* CMOS-compatible graphene photodetector covering all optical communication bands [J]. *Nature Photonics*, 2013, **7** (11), 892–896.
- [14] Principi A, Vignale G, Carrega M, *et al.* Impact of disorder on Dirac plasmon losses [J]. *Physical Review B*, 2013, **88** (12), 1405.
- [15] Ryzhii V, Ryzhii M. Graphene bilayer field-effect phototransistor for terahertz and infrared detection [J]. *Physical Review B*, 2009, **79** (24), 5311.
- [16] Dyakonov M, Shur M. Detection, mixing, and frequency multiplication of terahertz radiation by two-dimensional electronic fluid [J]. *IEEE Trans. Electron Devices*, 1996, **43** (3), 380–387.
- [17] Tomadin A, Polini M. Theory of the plasma-wave photoresponse of a gated graphene sheet [J]. *Physical Review B*, 2013, **88** (20), 5426.
- [18] Basko D. Applied physics. A photothermoelectric effect in graphene [J]. *Science*, 2011, **334** (6056), 610–611.
- [19] Cai X, Sushkov A B, Suess R J, *et al.* Sensitive room-temperature terahertz detection via the photothermoelectric effect in graphene [J]. *Nat Nanotechnol*, 2014, **9** (10), 814–819.
- [20] Zhai Y, Xiang Y, Yuan W, *et al.* Fabrication of Graphene Nanomesh FET Terahertz Detector [J]. *Micromachines (Basel)*, 2021, **12** (6), 641.
- [21] Liu C, Wang L, Chen X, *et al.* Room-temperature photoconduction assisted by hot-carriers in graphene for sub-terahertz detection [J]. *Carbon*, 2018, **130**, 233–240.
- [22] Huang Z, Tong J, Huang J, *et al.* Room-temperature photoconductivity far below the semiconductor bandgap [J]. *Adv Mater*, 2014, **26** (38), 6294–6598.
- [23] Huang Z, Zhou W, Tong J, *et al.* Extreme Sensitivity of Room-Temperature Photoelectric Effect for Terahertz Detection [J]. *Adv Mater*, 2016, **28** (1), 112–117.
- [24] Sakowicz M, Lifshits M B, Klimenko O A, *et al.* Terahertz responsivity of field effect transistors versus their static channel conductivity and loading effects [J]. *Journal of Applied Physics*, 2011, **110** (5), 054512.
- [25] Knap W, Dyakonov M, Coquillat D, *et al.* Field Effect Transistors for Terahertz Detection: Physics and First Imaging Applications [J]. *Journal of Infrared, Millimeter, and Terahertz Waves*, 2009, **30**: 1319–1337.
- [26] Tauk R, Teppe F, Boubanga S, *et al.* Plasma wave detection of terahertz radiation by silicon field effects transistors: Responsivity and noise equivalent power [J]. *Applied Physics Letters*, 2006, **89** (25), 253511.
- [27] Vicarelli L, Vitiello M S, Coquillat D, *et al.* Graphene field-effect transistors as room-temperature terahertz detectors [J]. *Nat Mater*, 2012, **11** (10), 865–871.
- [28] Castilla S, Terres B, Autore M, *et al.* Fast and Sensitive Terahertz Detection Using an Antenna-Integrated Graphene pn Junction [J]. *Nano Lett*, 2019, **19** (5), 2765–2773.
- [29] Wu C, Zhou W, Yao N, *et al.* Silicon-based high sensitivity of room-temperature microwave and sub-terahertz detector [J]. *Applied Physics Express*, 2019, **12** (5), 052013.
- [30] Weng Q, Komiyama S, Yang L, *et al.* Imaging of nonlocal hot-electron energy dissipation via shot noise [J]. *Science*, 2018, **360** (6390), 775–778.
- [31] Kampfrath T, Perfetti L, Schapper F, *et al.* Strongly coupled optical phonons in the ultrafast dynamics of the electronic energy and current relaxation in graphite [J]. *Phys Rev Lett*, 2005, **95** (18), 187403.
- [32] Alzahrani A Z, Srivastava G P. Gradual changes in electronic properties from graphene to graphite: first-principles calculations [J]. *J Phys Condens Matter*, 2009, **21** (49), 495503.
- [33] Stange A, Sohrt C, Yang L X, *et al.* Hot electron cooling in graphite: Supercollision versus hot phonon decay [J]. *Physical Review B*, 2015, **92** (18), 184303.
- [34] Asgari M, Riccardi E, Balci O, *et al.* Chip-Scalable, Room-Temperature, Zero-Bias, Graphene-Based Terahertz Detectors with Nanosecond Response Time [J]. *ACS Nano*, 2021, **15** (11), 17966–17976.
- [35] Zak A, Andersson M A, Bauer M, *et al.* Antenna-integrated 0.6 THz FET direct detectors based on CVD graphene [J]. *Nano Lett*, 2014, **14** (10), 5834–5838.
- [36] Viti L, Cadore A R, Yang X, *et al.* Thermoelectric graphene photodetectors with sub-nanosecond response times at terahertz frequencies [J]. *Nanophotonics*, 2020, **10** (1), 89–98.
- [37] Suzuki D, Okamoto T, Li J, *et al.* Terahertz and infrared response assisted by heat localization in nanoporous graphene [J]. *Carbon*, 2021, **173**, 403–409.